DOI: 10.1002/chem.201001211

X-ray Fluorescence Investigation of Ordered Intermetallic Phases as Electrocatalysts towards the Oxidation of Small Organic Molecules

Yi Liu,[a, b, c] Michael A. Lowe,[a, b, c] Ken D. Finkelstein,[c] Darren S. Dale,[c] Francis J. DiSalvo,[a, b] and Héctor D. Abruña*[a, b]

Abstract: The composition of ordered intermetallic nanoparticles (PtBi and PtPb) has been quantitatively studied by in situ X-ray fluorescence (XRF) during active electrochemical control in solutions of supporting electrolyte and small organic molecules (SOMs). Because the Pt $L_{\beta1,2}$ lines and the Bi $L_{\alpha1,2}$ lines are only separated by 200 eV, an energy-dispersive detector and a multiple-channel analyzer (MCA) were used to record the major fluorescent emission lines from these two elements. The molar ratios of platinum to the less-noble elements (Bi, Pb) in the nanoparticles dramatically changed as a function of the applied upper limit potentials (E_{ulp}) in cyclic voltammetric (CV) characterization. Similar to previous investigations for bulk intermetallic surfaces, the less-noble elements leached out from the surfaces of the intermetallic nanoparticles. For PtBi nanoparticles, the ratios of fluorescence intensities of Pt/Bi in the samples were 0.42, 0.96, and 1.36 for $E_{ulp} = +0.40$, $+0.80$, and 1.20 V, respectively, while cycling the potential from -0.20 V to the E_{ulp} value for 10 cycles. The leaching-out process of the less-noble elements occurred at more negative E_{ulp} values than expected. After cycling to relatively positive E_{ulp} values, nonuniform PtM (M = Bi of Pb) nanoparticles formed with a Pt-rich shell and intermetallic PtM core. When the supporting solutions contained active fuel molecules in addition to the intermetallic nanoparticles (formic acid for PtBi, formic acid and methanol for PtPb), kinetic stabilization effects were observed for $E_{ulp} = +0.80$ V, in a way similar to the response of the bulk materials. It was of great importance to quantitatively explore the change in composition and structure of the intermetallic nanoparticles under active electrochemical control. More importantly, this approach represents a simple, universal, and multifunctional method for the study of multi-element nanoparticles as electrocatalysts. This is, to our knowledge, the first report of nondestructive, quantitative characterization of bimetallic or multi-elemental nanoparticles electrocatalysts under active electrochemical control.

Keywords: electrocatalysts · fuel cells · intermetallic phases · nanoparticles · fluorescence spectroscopy

Introduction

In the general area of heterogeneous catalysts,[1,2] it is of great importance to characterize nanomaterial catalysts under operating conditions as such studies can provide an in-depth atomic-level understanding of the reaction mechanism or interfacial processes. Recent advances in functional catalytic materials and spectroscopic methods that can operate under ambient pressures now enable us to investigate a catalyst in its active state. Particularly for electrode materials for fuel cell applications, various surface/interface/nanomaterial characterization techniques, in combination with electrochemical characterization, allow monitoring of the transformation of electrocatalysts from the "as-prepared state" to the "active state", which may involve pronounced changes in the composition and structure of the catalysts.[3–6] X-ray diffraction (XRD) has been widely utilized to characterize the crystalline composition and structure of condensed matter at surfaces/interfaces (also known as grazing incidence diffraction, GID) where electrochemical reactions occur. However, it is very difficult for XRD to yield the appropriate information for short-range structures or amor-

[a] Dr. Y. Liu, M. A. Lowe, Prof. F. J. DiSalvo, Prof. H. D. Abruña
Baker Laboratory, Department of Chemistry and Chemical Biology
Cornell University
Ithaca, NY 14853-1301 (USA)
Fax: (+1) 607-255-9864
E-mail: hda1@cornell.edu

[b] Dr. Y. Liu, M. A. Lowe, Prof. F. J. DiSalvo, Prof. H. D. Abruña
Energy Materials Center at Cornell (EMC^2)
Ithaca, NY 14853 (USA)

[c] Dr. Y. Liu, M. A. Lowe, Dr. K. D. Finkelstein, Dr. D. S. Dale
Cornell High Energy Synchrotron Source (CHESS)
Ithaca, NY 14850 (USA)

phous phases of catalysts. For nanomaterial catalysts, one argument in favor of the utilization of XRD has been that the number of surface atoms is significant with respect to the number of atoms in the bulk; therefore, XRD data of such nanomaterial samples would be directly relevant to catalysis. Because this argument might be valid for other bulk-sensitive techniques, it does not work for XRD, because the structural uniformity of the bulk of a material does not pertain to the surfaces of nanoparticles. For example, surface reconstructions have major consequences on the average arrangement of surface atoms.[7,8] X-ray photoelectron spectroscopy is a powerful method with great surface sensitivity, and can offer qualitative or semi-quantitative composition and oxidation-state information, but its requirement of strict ultra-high vacuum does not permit active electrochemical control.[9] X-ray absorption spectroscopy (XAS), including X-ray absorption near edge structure (XANES) and extended X-ray absorption fine structure (EXAFS), has attracted a great deal of research attention, especially for analysis and characterization of catalysts.[6,10–12] XAS provides element-specific information about the local chemistry and physical structure of the element under investigation. XANES offers information about the chemical state of the element, including oxidation state and local geometry, and EXAFS offers quantitative information about interatomic distances, coordination numbers, and the types of neighboring atoms. XAS is a valuable method to investigate short-range order and is especially suitable for nanomaterials. A disadvantage of XAS (or EXAFS) is that sophisticated and complicated data analysis and simulation are required, especially when the element of interest is present in multiple oxidation states and multiple local chemical environments, which can be difficult to disentangle.

X-ray fluorescence (XRF) is a widely used analytical technique employed in different fields,[13–15] such as environmental studies,[16] medicine,[17] polymers,[18] biology,[19] botany,[20] archeology,[21] pharmacology,[22] and planetary studies.[23] Attractive features of the XRF technique include the fact that it is nondestructive, has high elemental selectivity, simplicity of quantification, and low detection limits. There have been studies on the application of XRF in combination with electrochemistry for the characterization of surface species, nanoparticles and nanowires, or indirectly in catalyst research. For example, De Wael and co-workers[24] reported on a study in which they used scanning synchrotron radiation X-ray fluorescence (SR-XRF), on the microscopic scale, to characterize the immobilization of cobalt(II) tetrasulfonated phthalocyanine tetrasodium salt (Co^{II}TSPc) on gold electrodes through different electrochemical surface modification techniques. Electrochemical and SR-XRF analysis were performed to compare the amount of adsorbed CoTSPc onto the gold electrode and to determine the level of uniformity of the deposited layer. Van Meel and co-workers[25] developed a fast and direct determination procedure for precious metals (such as Pt, Pd, and Rh) in spent automotive catalysts by using the novel high-energy polarized-beam XRF technique. Wang and co-workers[26] developed a barcoding procedure for alloy nanowires based on nondestructive X-ray fluorescence readout. Ternary Co-Ni-Cu alloy nanowires were generated by one-step template-guided electrodeposition with distinct XRF barcode patterns. The resulting fluorescence barcodes correlated well with the composition of the metal mixture plating solution, indicating a reproducible plating process. To our knowledge, there is no report on methodology development or application of nondestructive XRF to directly characterize nanomaterials electrocatalysts for fuel cell applications, especially under active electrochemical control.

In the past decades, interest in the direct conversion of chemical energy to electricity through fuel cells has received increasing attention. The use of fuel cells can circumvent Carnot cycle limitations and can, in principle, supply energy with conversion efficiencies in excess of 80%, depending on the fuel used.[27] Due to increasing demands of power sources for small portable electronic devices, the development and utilization of direct alcohol fuel cells (DAFCs) has attracted a great deal of research interest.[28–30] Some of the major obstacles relate to the performance and cost of anode and cathode electrocatalysts.[31] It is of great importance to develop advanced functional materials as anode catalysts for oxidations of small organic molecules (SOMs). Platinum is an excellent catalyst for dehydrogenation of fuels, which is one of the key steps in the complete oxidation reaction pathways of SOMs. However, Pt is easily poisoned by carbon monoxide, which is the most common intermediate during SOM oxidation. In order to mitigate the poisoning effects induced by CO and to decrease the cost of electrode materials, a secondary metallic element is often introduced into the matrix to form bimetallic electrocatalysts. PtRu alloys represent the most successful case and are widely used in the fuel cell industry, especially for direct methanol fuel cells. Their success has been rationalized by a bifunctional mechanism and/or third body effect.[32,33] Unfortunately, as with all alloys, or more accurately solid solutions, PtRu electrodes have no well-defined surface structure, with their surface sites occupied by Pt or Ru atoms in a totally random mode. Moreover, the very small enthalpy of formation of PtRu alloys leads to a thermodynamic stability problem: during extended periods of operation, particularly under high-temperature or high-current-density conditions, the alloy electrode surface is depleted of Ru atoms, loses electrocatalytic activity and is prone to poisoning by CO.

Ordered intermetallic phases exhibit inherent properties that overcome many of the shortcomings of alloy materials. Intermetallics are binary or multi-elemental metallic compounds, which have well-defined crystalline structures. In principle, the electronic and atomic structures, both of which are widely acknowledged to be important parameters in electrocatalytic activity, can be deliberately controlled. DiSalvo, Abruña, and co-workers[34,35] reported that ordered intermetallic PtBi and PtPb phases were promising candidates towards the oxidation of formic acid and methanol in comparison to commercial Pt and PtRu materials. Not only do they exhibit greatly enhanced electrocatalytic activity

(especially relative to Pt), but they could also serve as model systems to explore structure/composition/property/activity relationships. Control of surface termination, composition, and structure of the intermetallic phases provide alternatives to fabricate modified single-crystal metal surfaces through electrodeposition or bimetallic single-crystal surfaces generated by chemical vapor deposition or sputtering methods.[36] Previous research has demonstrated that polycrystalline PtBi intermetallic electrodes can be reproducibly terminated with Pt nanocrystal domains decorating the surface after cycling the potential or with a Bi_2O_3 2D nanocrystalline film decorating the surface after holding the potential at specified values. In the case of PtPb, Pt nanocrystal domains were formed on the surface through both treatments (cycling and holding the potential) although the later treatment could induce aggressive corrosion of the top PtPb layers.[37,38] On single-crystal electrodes, Pt nano-islands with 6-fold hexagonal or 2-fold rectangular symmetries were formed on the PtM (M = Bi or Pb) (001) and (100) surfaces, respectively, instead of formation of random Pt nanocrystal domains/islands as with the polycrystalline intermetallic phases.[36] Whereas the work on single-crystal intermetallic surfaces has been important to reveal structure–activity relationships, it is of more practical importance to characterize intermetallic nanomaterial samples because they are directly used in industrial applications.

In this paper, XRF was utilized to quantitatively investigate and characterize intermetallic nanoparticles. X-ray diffraction, though powerful, has some limitations in the characterization of these materials, because of: 1) low diffraction intensities of nanoparticles immobilized on electrode surfaces, such as glassy carbon, even when using a high flux synchrotron beam; 2) strong back scattering from the glassy carbon (GC) electrode surface at grazing incidence; and 3) inability of obtaining information of the surface atoms instead of the bulk. XRF data showed that there were significant changes in the composition of PtBi and PtPb nanoparticles, as a function of applied potential, in absence or presence of fuel molecules in the supporting electrolyte. PtM/Pt core/shell nanoparticles were formed as a consequence of the less-noble element (Bi or Pb) leaching out from the nanoparticle matrix and dissolving into the solution. Similar to bulk electrodes,[38] kinetic stabilization effects, induced by the presence of active fuel molecules, were also observed for the intermetallic nanoparticles. More importantly, a universal simplified nondestructive multifunctional characterization method was developed to investigate bimetallic electrocatalysts, especially under active electrochemical control.

Results and Discussion

XRF multi-channel analyzer (MCA) spectra of PtBi and PtPb nanoparticles: The energy resolutions of the VORTEX and X-Flash detectors were not sufficient to completely separate the X-ray emission lines from Pt L_β and Bi L_α when the incident beam energy was higher than 13.42 keV. In order to get accurate fluorescent emission intensities of specific elements in the nanoparticles, under active electrochemical control, the entire MCA spectrum was recorded with the VORTEX detector.

As mentioned earlier, for PtBi nanoparticles the energy scan started from 13.30 KeV, which is below the binding energy of the Bi L_3 edge. The fluorescent signals were coming from Pt emission lines and were dominated by the Pt L_α (9.44 keV) and the Pt L_β (11.07 keV) emission lines (see Table 1). Bismuth fluorescence signals increased after scanning the energy past 13.42 keV, that is, the Bi L_3 absorption edge. For PtPb nanoparticles the energy scan started from 12.95 keV, which is below the binding energy of the Pb L_3 edge. The Pb fluorescent signals were evident after scanning the energy past 13.04 keV, that is, the Pb L_3 absorption edge. Figure 1 presents a typical Bi L_α fluorescence spectrum recorded by the single-channel analyzer (SCA) window, which was deliberately set up to cover the range of Bi L_α fluorescent photons. There were two steps in the XRF intensities at 13.42 keV and 13.88 keV, respectively, corresponding to the energies of the Bi L_3 and Pt L_1 absorption edges. The small step at 13.88 keV, ascribed to the Pt L_1 absorption edge, was unexpected and surprising because only Pt L_β emissions, with energies of 13.27 (Pt L_2 edge) or 11.56 keV (Pt L_1 edge), could be detected by the SCA window. There are two possible reasons for this phenomen-

Table 1. Relevant binding energies and emission lines of Pt, Bi, and Pb.[42]

	Binding energy [keV]			Emission energy [keV]			
	L_1	L_2	L_3	$L_{\alpha1}$	$L_{\alpha2}$	$L_{\beta1}$	$L_{\beta2}$
Pt	13.88	13.27	11.56	9.44	9.36	11.07	11.25
Bi	16.39	15.71	13.42	10.84	10.73	13.02	12.98
Pb	15.86	15.20	13.04	10.55	10.45	12.61	12.62

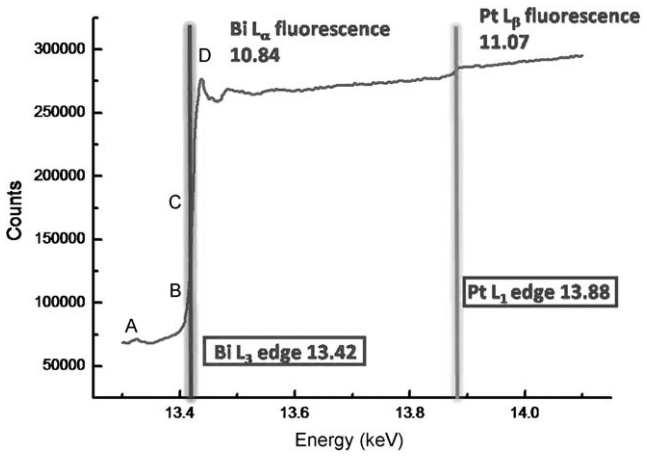

Figure 1. A typical energy scan recorded by the single-channel analyzer SCA window for a PtBi-nanoparticle-modified electrode. The marks of A, B, C, and D correspond to MCA scans in Figure 2.

on: 1) there is an unknown Pt fluorescence emission directly associated with the Pt L_1 edge at 13.88 keV; 2) there is a complex process involving nonradiative energy dissipation to give Pt L_β emission associated with the initial excitation of 13.88 keV. In order to figure out the origin of this fluorescence process ascribed to the Pt L_1 edge in Figure 1, the MCA spectra was recorded and post-experimental simulation and fitting data analysis based on the XPaXs software[39] were carried out. If the first assertion was correct, a new fluorescence peak would appear in the MCA spectra once the energy passed by 13.88 keV. If the nonradiative process is the correct explanation, rather than the appearance of a new emission peak, the intensity of the Pt L_β emission should increase as the energy is scanned past 13.88 keV. As shown in Figure 2, the MCA spectra obtained before and after the binding energy of the Pt L_1 edge strongly suggest

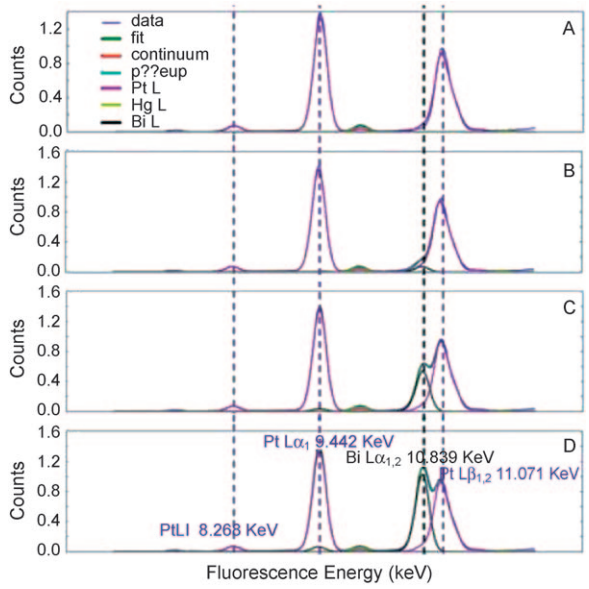

Figure 2. MCA scans for a PtBi-nanoparticle-modified electrode recorded by the VORTEX detector. The relationship between the different incident energies for the different panels are also indicated in Figure 1.

that the second explanation is likely responsible for the observed phenomenon. In essence, there was no new peak detected in the MCA spectra after scanning the energy past 13.88 keV. Instead, the intensity of the Pt L_β fluorescence peak increased. Although a bit speculative on our part, we believe that Pt L_1 electrons are ejected by the 13.88 keV incident photons generating holes on the L_1 level. Electrons from the Pt L_2 and L_3 levels filled the holes (on the Pt L_1 level) by intra-atomic relaxation and the extra energy was dissipated by a nonradiative process. Then, electrons from higher levels, like Pt M_4 or N_5, jumped into the holes left on the Pt L_2 and L_3 levels to generate more Pt L_β fluorescent photons.

Figure 2 shows four images (A, B, C, and D) of MCA spectra corresponding to four different representative positions in a typical energy scan, such as in Figure 1. Scan A was recorded at an energy below the Bi L_3 absorption edge, scan B was detected at the foot of the rising Bi L_α fluorescence emission, scan C was recorded at the middle of the Bi L_3 absorption edge, and scan D was recorded just over the Bi L_3 absorption edge. In Figure 2, the *x* axis represents energies of photons which went into the VORTEX detector and were recorded by the MCA with 1200 channels (for a representation of the experimental set up, see Figure 3). The experimental data were fitted with the XPaXs software following the optimization of parameters such as detector calibration, thickness of the nanoparticle sample, substrate properties, distance between the detector and sample, attenuation factor in front of the detector, and others. The simulations of possible emission peaks, corresponding to different elements, are presented in different colors. The Pt L_1, L_α and L_β emissions were consistently present in the A, B, and C scans because all of these peaks were excited at the beginning of the energy scan. From the B, C, and D scans, the increasing trend of the Bi L_α emission is clearly evident as the energy passed over the Bi L_3 absorption edge at 13.42 keV. Based on the simulations of fluorescence peaks from the different elements, precise XRF intensities corresponding to each element and each specific emission could be obtained without interference and a quantitative analysis is presented below.

Quantitative characterization for the leaching-out process of the less-noble metals based on XRF data: It is of great importance to characterize the changes in composition and structure of intermetallic nanoparticles, because these would be the actual phases for commercial and industrial applications. As stated previously, X-ray diffraction, a conventional characterization method for the bulk or the surfaces of elec-

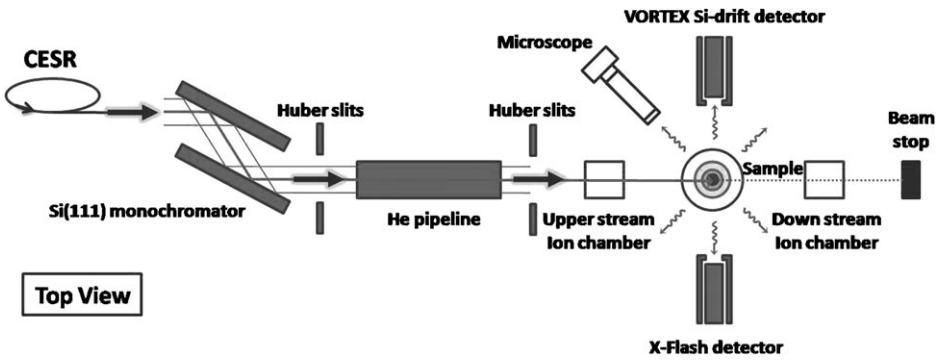

Figure 3. Schematic representation of the experimental geometry used for the X-ray fluorescence experiments at the C1 station at the Cornell High Energy Synchrotron Source (CHESS).

trocatalysts under active potential control, is not suitable for in situ measurement of nanoparticles. The amount of immobilized nanoparticles (80 $\mu g\,cm^{-2}$) on the substrate of the GC electrode, which was optimized for electrocatalytic activity, did not give detectable diffraction signals, even when using the well-established grazing incidence diffraction method. Moreover, the substrate GC electrode gave strong and broad backscattering peaks, which covered the two theta range corresponding to the major diffraction peaks of PtBi and PtPb intermetallic phases. Thus, neither XRD nor GID methods could be utilized to characterize these nanoparticles under active electrochemical control. In previous studies, we have shown that the composition and structure of intermetallic surfaces in either polycrystalline or single-crystal forms, dramatically changed as a function of applied potential. Different electrochemical pretreatment methods, such as cycling versus holding the potential, gave rise to differently terminated surfaces. The results from in situ GID or XRD investigations were qualitative or, at best, semiquantitative. Here, changes in the composition of the nanoparticles were determined in a more quantitative way by the XRF method. Specific energy scans to acquire XRF data were carried out for a freshly prepared nanoparticles-modified electrode and after cycling the electrode to potentials between -0.20 V and the upper limit potential (E_{ulp}) for 10 cycles in aqueous $HClO_4$ (0.1 M). As mentioned above, in order to obtain precise intensities for each emission peak of specific elements, XRF data were extracted from simulations of experimental records through MCA spectra. At the same time, the pseudo SCA window recorded mainly the Bi L_α fluorescence with some contribution from the L_β fluorescence. As shown in Figure 4, we made use of XRF data obtained through the SCA window to get quantitative information about molar ratios of Pt to Bi in the nanoparticles. From Figure 4 we could derive the Pt/Bi ratios of fluorescence, which were 0.42, 0.96, and 1.36 for E_{ulp} values of $+0.40$, $+0.80$, and $+1.20$ V, respectively. These results suggest that the Bi leaching-out process from the nanoparticles occurred at more negative E_{ulp} values than for bulk intermetallic phases. Because the XRF experiment was carried out at incidence angle of $\approx$1–2°, and the thickness of the nanoparticles-modified layer on the GC electrode was $\approx$50 μm, almost the entire layer of nanoparticles on the working electrode was sampled under this experimental condition. It should be kept in mind that the fluorescence signals favored information about the surface composition of the nanoparticles instead of that of the entire nanoparticles. The ratios of fluorescence intensities of Pt to Bi of the intermetallic PtBi nanoparticles increased as a function of applied E_{ulp}, indicating that the bismuth atoms gradually leached out from the surfaces of the nanoparticles while cycling the potentials to increasingly positive values in the supporting electrolyte. As a result, the surfaces became enriched in Pt after these electrochemical pretreatments. The nanoparticles were essentially changed from uniform composition intermetallic nanoparticle to a core/shell nanostructure with an intact intermetallic PtBi phase at the core and a Pt-rich outmost layer of

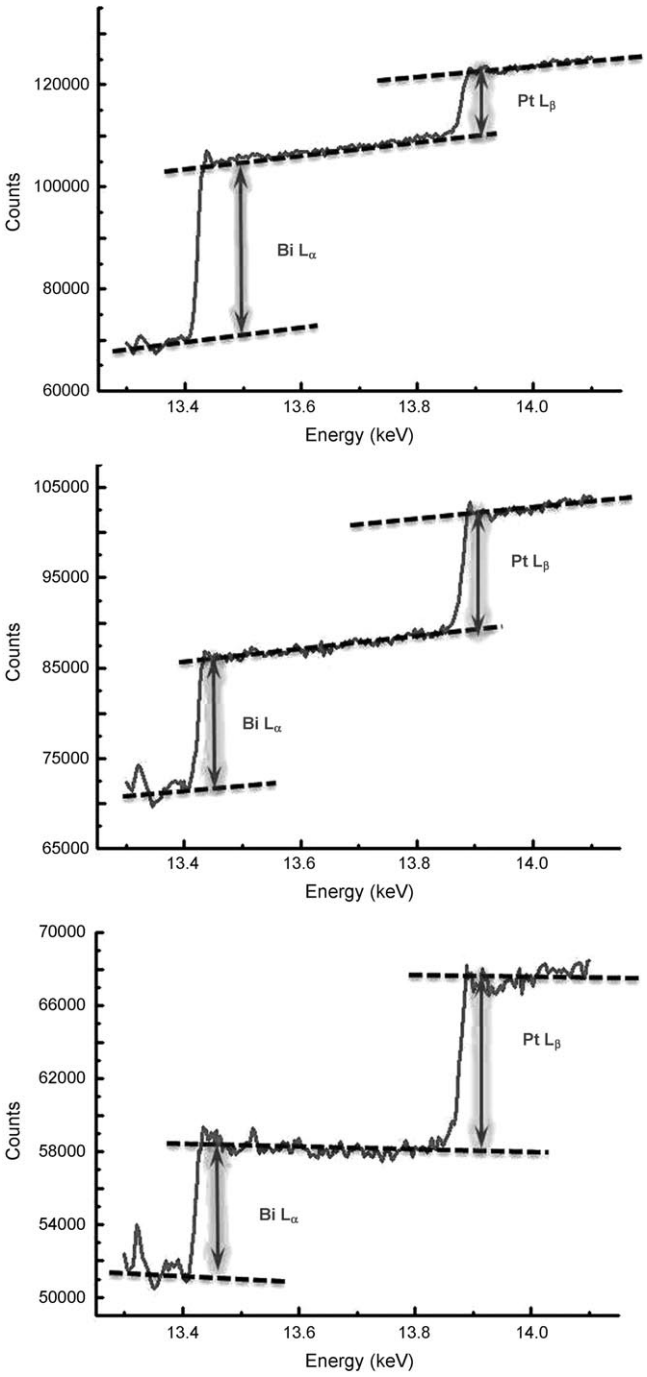

Figure 4. Scans depicting changes in the ratios of fluorescence intensities of Pt to Bi in the nanoparticles as a function of applied E_{ulp} values of $+0.40$ (top), $+0.80$ (middle), and $+1.20$ V (bottom) in the supporting electrolyte, based on quantitative analysis of XRF data.

PtBi phase as the shell. Similar behavior was also observed for intermetallic PtPb-nanoparticle-modified electrodes, with the only difference being that the working electrode was subjected to electrochemical pretreatment by holding (not scanning) the potential. Figure 5 shows pseudo-2D-mapping images of XRF data for PtPb nanoparticles while holding the potential at $+0.40$ and $+0.80$ V in aqueous

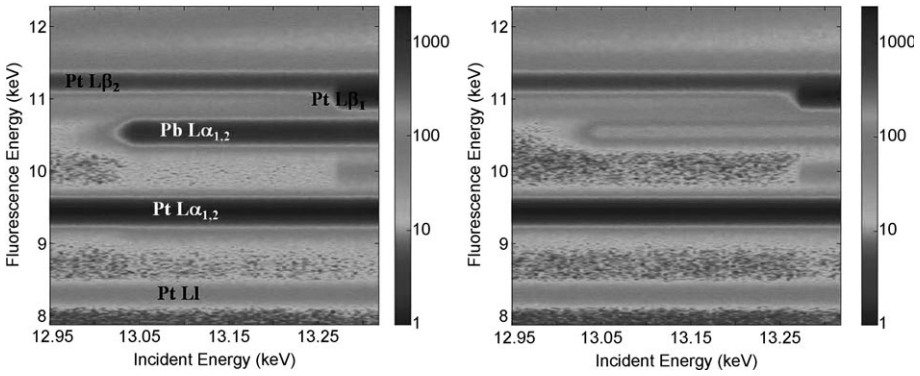

Figure 5. Intensity maps of the fluorescence spectra versus incident energy for PtPb nanoparticles as a function of applied E_{ulp} of +0.40 (left) and +0.80 V (right) in the supporting electrolyte.

$HClO_4$ (0.1 M). The 2D-mapping images provide more detailed information of intensities for each emission peak of a specific element in a quantitative way. Each line in a 2D-mapping image represents an individual emission line from a specific element. Whereas there was little change in fluorescence intensities emissions from Pt atoms, the intensity of the Pb L_α emission decreased dramatically. Thus, Pb was clearly leached out from the nanoparticle sample by increasing the applied potential and ostensibly gave rise to Pt shell/PtPb core nanoparticles. Because the absolute intensities of the Pt fluorescence changed little for applied potentials of +0.40 and +0.80 V, one would expect that the diameter of the nanoparticles likely decreased extensively as a consequence of the leaching-out process of Pb. More discussion about XRF data extracted from MCA spectra will be extensively discussed elsewhere in the future.

Kinetic stabilization of intermetallic nanoparticles phases: We have previously documented kinetic stabilization effects induced by active fuel molecules present in solution for bulk electrodes of PtBi and PtPb intermetallic phases.[38] XRF experiments that were carried out to determine such kinetic stabilization effects are now presented for intermetallic nanoparticle phases. Figure 6 presents XRF data for a PtBi-nanoparticle-modified electrode while cycling the E_{ulp} to +0.80 V in the absence (Figure 6a) or presence (Figure 6b) of formic acid in the supporting electrolyte. The Pt/Bi fluorescence intensity ratios were 0.19 and 0.96 in aqueous solution of HCOOH (0.2 M)/H_2SO_4 (0.1 M) and in aqueous H_2SO_4 (0.1 M) , respectively. In the former case, the Bi leaching-out process was precluded by the PtBi-catalyzed oxidation of formic acid, whereas the latter involved the corrosion/oxidation of the nanoparticles themselves. These results are very similar to those for bulk electrodes but in this case, we could obtain more quantitative data. The fluorescence intensity ratio of Pt/Bi of 0.19 for cycling the E_{ulp} to +0.80 V in aqueous solution of HCOOH (0.2 M)/ H_2SO_4 (0.1 M) was much lower than that for cycling the E_{ulp} to +0.40 V in aqueous H_2SO_4 (0.1 M) (i.e., 0.42). Two main conclusion could be derived: 1) aggressive leaching out of Bi occurred even for an E_{ulp} value of +0.40 V, which is 400 mV more negative as the results obtained from qualitative GID/XRD characterizations, and 2) the leaching-out process of Bi from PtBi nanoparticles was completely precluded at an E_{ulp} value of +0.80 V in the presence of formic acid in the supporting electrolyte. Figure 7 presents pseudo-2D-mapping images of XRF data for PtBi nanoparticles for holding potentials of +0.40 and +1.20 V for 10 min in aqueous solution of HCOOH

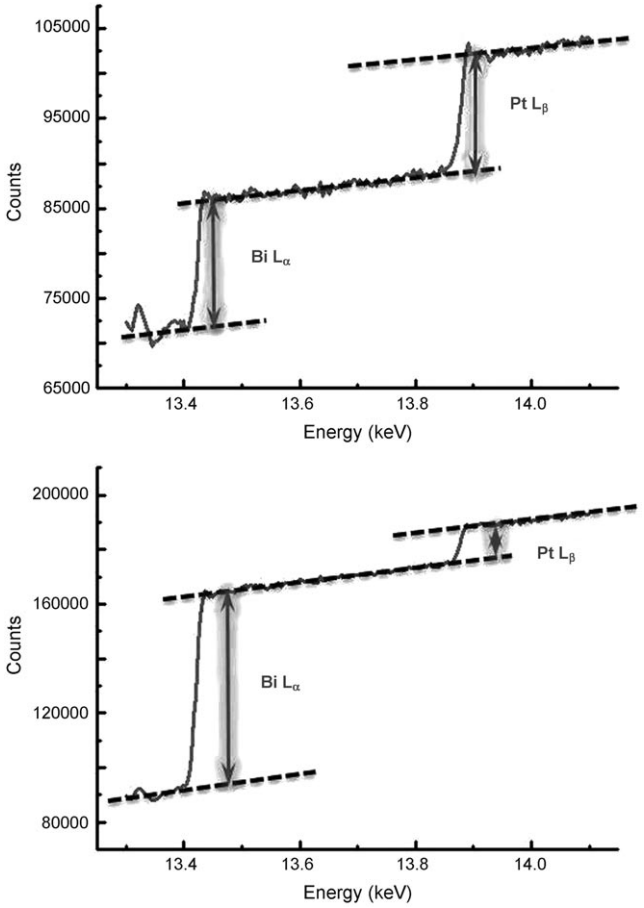

Figure 6. Scans depicting changes in the ratios of fluorescence intensities of Pt to Bi from PtBi nanoparticles after cycling to an E_{ulp} value of +0.80 V in the absence (top) and presence (bottom) of formic acid in the supporting electrolyte, based on quantitative analysis of XRF data.

(0.2 M)/H_2SO_4 (0.1 M). Particular attention was paid to the changes in the fluorescence intensities of Pt and Bi emissions and the Pt/Bi ratios at different E_{ulp} values. The intensity of the Bi L_α emission decreased slightly (less than 10%) while increasing the holding potential from +0.40 to +1.20 V and there were very small changes in the intensities

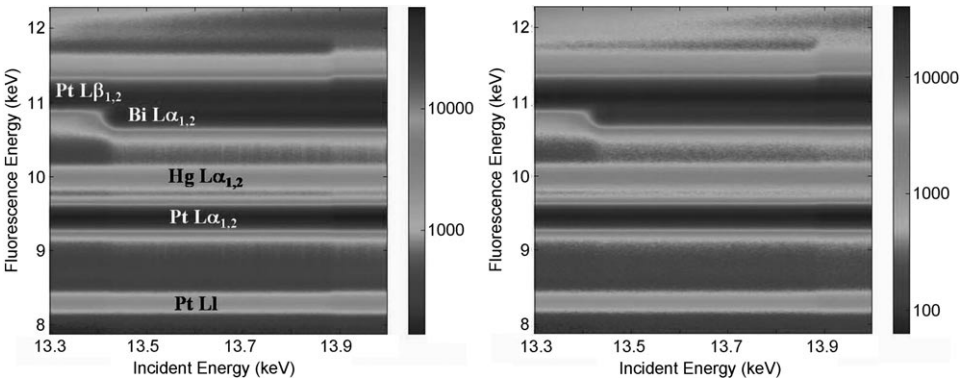

Figure 7. Intensity maps of fluorescence spectra versus incident energy for PtBi nanoparticles as a function of applied E_{ulp} of +0.40 (left) and +1.20 V (right) in the presence of formic acid in the supporting electrolyte.

of the Pt emission lines during electrochemical treatments. This suggests that whereas kinetic stabilization effects are observed for PtBi nanoparticles under these conditions, at the same time bismuth starts to leach out from the matrix when the E_{ulp} value is +1.20 V. This potential also corresponds to the potential at which the formic acid molecules are fully oxidized and the surface corrosion of the nanoparticles is enabled.

EXAFS and XANES characterization of the Bi L_3 edge from PtBi nanoparticles: There were two ways to obtain EXAFS and XANES spectra from our XRF experimental geometry: 1) directly recorded through the SCA detector, 2) recompile the spectrum from the XRF data extracted from the MCA scan after special data analysis by XPaXs software. Figure 8 presents the EXAFS and XANES spectra obtained through the SCA detector while cycling to different E_{ulp} values of +0.40, +0.60, +0.80, +1.00, and +1.20 V in aqueous H_2SO_4 (0.1 M). As is evident, the EXAFS spectra exhibited little change during electrochemical pretreatments. In the XANES spectra, the Bi L_3 edge absorption edge shifted to higher energy while cycling of the potential to any positive value when compared to a freshly prepared electrode. This indicates that bismuth atoms on the surfaces of the nanoparticles are oxidized as the binding energy (absorption edge) shifts to higher value. Besides the sudden change in adsorption edge from freshly prepared electrodes to electrodes cycled to E_{ulp} = +0.40 V, there was little change in the XANES spectra. The little change of the absorption edges in the XANES spectra as a function of applied potentials indicates that the initial oxidized bismuth species induced by E_{ulp} = +0.40 V will not be further oxidized to higher chemical oxidation states. Although there is little change of oscillation patterns in the EXAFS data as a function of applied potentials, it is not rational to believe that the local chemical environment of the bismuth atoms has little changed after the formation of core/shell nanostructure induced by bismuth leaching-out process. The reason we did not observe the possible change in EXAFS data might be due to two aspects: 1) the interference with the Pt L_β emission to this EXAFS data recorded from SCA detector, especially after the bismuth leaching-out process the Pt/Bi molar ratio increases, 2) the change of local chemical environment for bismuth atoms is not aggressive enough to rise up to obvious feature change in EXAFS oscillation pattern. A more complete analysis of EXAFS and XANES data as a function of applied potential will be presented elsewhere.

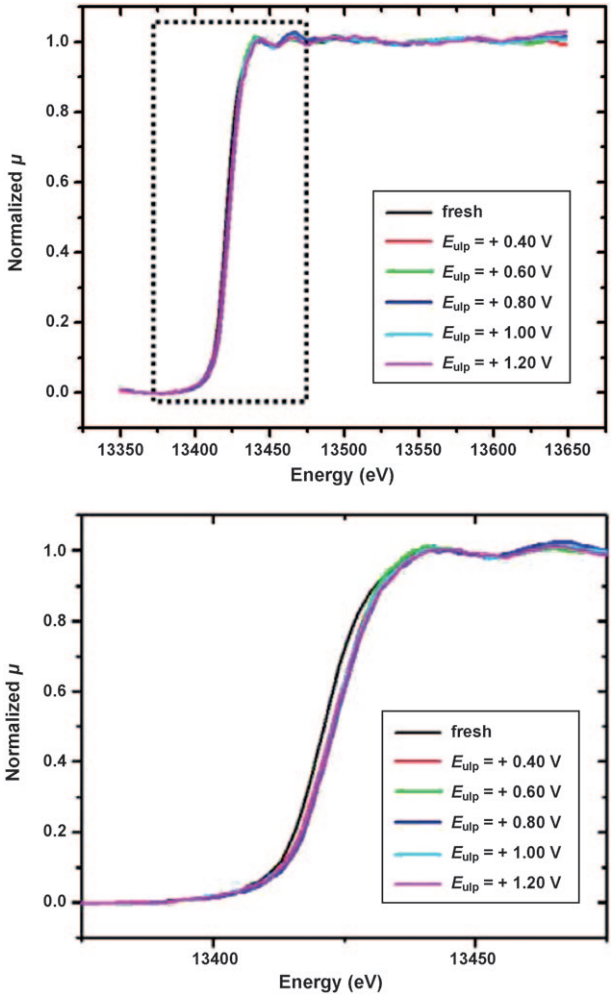

Figure 8. EXAFS (top) and XANES (bottom) spectra of the Bi L_3 edge from PtBi nanoparticles directly recorded by the SCA detector while cycling the E_{ulp} to different values in aqueous H_2SO_4 (0.1 M).

Conclusion

A simple, general use, multifunctional and nondestructive XRF method was developed to characterize the composition and structure of intermetallic PtBi and PtPb nanoparticles as electrocatalysts under active electrochemical control. SCA data derived from the conventional XFlash detector and MCA spectra recorded by the VORTEX detector were utilized to yield either quantitative XRF information or EXAFS and XANES spectra. Similar to solid-state electrodes investigated by qualitative or semiquantitative XRD or GID methods, the less-noble elements (Bi or Pb) were leached out from the intermetallic nanoparticles while cycling or holding the potential to positive values in the supporting electrolyte only. The leaching-out process was initially detected at $E_{ulp} = +0.40$ V, which is much more negative than expected based on previous studies on bulk samples. The core/shell structures were formed after certain electrochemical pretreatments and the diameters of the nanoparticles significantly decreased. Kinetic stabilization effects induced by active fuel molecules present in solution were observed for these nanoparticles in a way analogous to observations on bulk samples of these materials. EXAFS and XANES data showed that surface bismuth atoms in the nanoparticles were oxidized once the electrode was subjected to applied E_{ulp} values as low as $+0.40$ V and the oxidation state of Bi changed little as a function of applied potential to more positive values. Whereas our studies were conducted on PtBi and PtPb nanoparticles, this method could be generally utilized to characterize any bimetallic or multielemental electrocatalytic nanoparticles, especially samples in which there could be interference from the fluorescence emission from different elements.

Experimental Section

Synthesis of ordered intermetallic PtBi and PtPb nanoparticles: With the exception of Bi and Pb precursors, all materials used were reagent grade. $Bi(MOEEAA)_3$, as Bi precursor, was prepared by reacting stoichiometric amounts of bismuth acetate (99.999%, Alfa Aesar) and (2-[2-{2-methoxyl}ethoxy]ethoxy) acetic acid (MOEEAA) (Aldrich). The final product was purified and collected as a colorless, viscous liquid and stored in an argon-filled glovebox. $Pb(MOEEAA)_2$, as lead precursor, was prepared in the same way, by using lead acetate (Aldrich) as the starting material. Anhydrous methanol was degassed with argon for over 2 h. To synthesize intermetallic PtBi nanoparticles, $Bi(MOEAA)_3$ (0.25 g) was dissolved in degassed methanol. A stoichiometric amount, relative to the bismuth precursor, of $H_2PtCl_6{\cdot}6H_2O$ (as platinum precursor), was dissolved in degassed anhydrous methanol (10 mL) and added to the bismuth precursor solution. $NaBH_4$ (0.3 g) was dissolved in degassed anhydrous methanol (15 mL). This solution was immediately added to the metal precursor solution. There was instant bubbling, and a black product formed, which precipitated out of the solution within 10 min. The clear solution and the black product were stirred under argon for 12 h. The solid product was then separated from the supernatant liquid by decantation and centrifugation. It was subsequently rinsed with distilled water (3×) and acetone (3×) in order to remove the side products. Afterward, the powder was dried under vacuum at room temperature. PtPb intermetallic nanoparticles were prepared in the same way as described above, with the exception of using the lead precursor. More detailed information about synthesis and standard characterizations of these intermetallic nanoparticles can be found elsewhere.[40]

Electrochemistry: To obtain nanoparticle-modified electrodes, a suspension of the nanoparticle catalysts (referred to as nanoparticle ink) was firstly prepared as follows: The dried PtBi or PtPb nanoparticle sample (4 mg) were dissolved in Millipore water (3980 μL, 18.2 $M\Omega\,cm^{-1}$, Millipore Milli-Q) and isopropyl alcohol (1000 μL, Aldrich). Additionally, a Nafion solution in alcohols (20 μL, 5% w/w, Aldrich) was added to this mixture. The resulting mixture was sonicated in a bath-type ultrasonicator for at least 30 min. Each nanoparticle ink described above was coated onto a 5 mm diameter glassy carbon (GC) electrode by a simple drop-casting method. The GC electrode that served as the supporting substrate electrode was previously polished with 800 and 1200 Grit sandpapers (Buehler) for 15 min, respectively. The final polishing procedure was carried out by using 1 μm diamond paste suspended in a suitable extender (MetadiBuehler) for 15 min. The smooth GC electrode was then rinsed with Millipore water and allowed to dry in air. The modified working electrode was obtained by coating the intermetallic nanoparticles (80 $\mu g\,cm^{-2}$, 20 μL of nanoparticle ink) and then dried under nitrogen. All electrochemical characterizations were carried out in an in situ electrochemical cell deliberately designed for in situ synchrotron radiation X-ray techniques, which was sealed with a 5 μm polypropylene film in order to minimize X-ray absorption and back scattering effects.[37] Cyclic voltammetry was carried out with a BAS CV-27 potentiostat/galvanostat (Bioanalytical Systems) and recorded on a computer through a PCI-DAQ card (National Instruments). All potentials are referenced to a Ag/AgCl (saturated NaCl) electrode without regard for the liquid junction potential. The electrochemical pretreatment was done by cycling the electrodes between -0.20 V and E_{ulp} values of $+0.40$–$+1.20$ V for 10 cycles at 10 $mV\,s^{-1}$ in aqueous $HClO_4$ (0.1 M) (Aldrich, ultrapure reagent). SOMs oxidations at the nanoparticle-modified GC electrodes were examined in a mixture of formic acid (0.2 M, Mallinckrodt, 88% analytical reagent) or methanol (0.2 M, Aldrich) in aqueous $HClO_4$ (0.1 M) at a sweep rate of 10 $mV\,s^{-1}$ for 10 cycles. All solutions were prepared with Millipore water and deaerated with high-purity nitrogen for at least 15 min before each experiment.

Synchrotron radiation XRF: SR-XRF experiments were performed at the C1 station of the Cornell High Energy Synchrotron Source (CHESS). This beamline supports X-ray absorption and fluorescence experiments by using either "white" or monochromatic radiation with photon energies ranging from 5–50 keV. Figure 3 shows the experimental geometry used for our SR-XRF experiments, which also allowed for XANES and/or EXAFS investigations in grazing incidence surface fluorescence mode for solid-state samples or conventional transmission mode for nanoparticle samples. The white beam from the Cornell Electron Storage Ring (CESR) was monochromatized by a Si(111) double-bounce monochromator. The incident beam was defined by a set of Huber slits to be $1 \times 1\,mm^2$ in size and the incidence intensity was monitored by an upper stream ion chamber. The X-ray beam impinged on the electrode surface with an incidence angle of 1°. This small glancing angle was purposely chosen to maximize the electrode area under the beam radiation and minimize the background scatter from the GC electrode substrate. Two energy-dispersive silicon drift detectors, one a VORTEX detector and the other an X-Flash detector, were set up to record the fluorescent photons from the intermetallic nanoparticles. For the PtBi nanoparticle case, a SCA was used to monitor mainly the Bi L_α fluorescent photons detected by the XFlash detector at 10.84 keV and distinguish them from the Pt L_β fluorescent photons at 11.07 keV. Table 1 presents the relevant binding energies and emission lines for Pt, Bi, and Pb. Table 2 presents the detailed information of the X-ray transitions that give rise to the X-ray emission lines for Pt, Bi, and Pb used in the experiments and data analysis. Due to the small energy difference between the Bi L_α and Pt L_β emissions and the energy resolution of the detectors, the SCA window could not completely discriminate between them and only provided a qualitative analysis of the Bi fluorescence. This SCA window, by the XFlash detector, was used not only for experimental convenience, to directly monitor the progress of the energy scans, but also to obtain EXAFS and XANES information for the Bi L_3 edge. At the same time, the entire MCA spectrum was recorded by the VORTEX detector including the

Table 2. Transitions giving rise to the relevant Pt, Bi, and Pb emission lines.[42]

Labels	Transitions	Binding energy [keV]	Emission energy [keV]	Relative intensity
$L_{\alpha1}$	M_5–L_3	Pt 11.56	9.44	100
		Bi 13.42	10.84	100
		Pb 13.04	10.55	100
$L_{\alpha2}$	M_4–L_3	Pt 11.56	9.36	11
		Bi 13.42	10.73	11
		Pb 13.04	10.45	11
$L_{\beta1}$	M_4–L_2	Pt 13.27	11.07	67
		Pt 11.56	11.25	23
$L_{\beta2}$	N_5–L_3	Bi 13.42	12.98	25
		Pb 13.04	12.62	25
L_1	M_1–L_3	Pt 11.56	8.27	5

dispersive energy range for all fluorescent, scattered, and incident photons, to give accurate and specific photon counts for XRF investigations for postexperimental data analysis by using the PyMCA library.[41] For PtPb nanoparticles, the only difference was the set-up condition of the SCA window covering the Pb L_α emission. For combing X-ray characterization with electrochemistry, electrodes were pretreated by cycling 10 times between −0.20 V and the E_{ulp} values Subsequently, part of the supporting electrolyte solution was withdrawn so that the polypropylene film was recessed, generating a thin film of electrolyte as described above. The electrolyte film, however, was sufficiently thick to ensure good potential control in all cases. For PtBi-nanoparticle-modified electrodes, the energy scan was carried out from 13.3 keV, which is 120 eV lower than the binding energy of Bi L_1, to 14.0 keV, which is 580 eV above the binding energy of Bi L_3 and also higher than the binding energy of Pt L_1. The photon energy range was selected to obtain quantitative X-ray fluorescence emission from both bismuth and platinum and, at the same time, EXAFS and XANES information across the bismuth L_3 adsorption edge. For PtPb-nanoparticle-modified electrodes, the energy scan was performed from 12.95 keV, which is 80 eV below the binding energy of Pb L_3, to 13.30 keV, which is 350 eV above the binding energy of Bi L_1, and also higher than the binding energy of Pt L_2. Each energy scan took about 15 min and 10 scans were average to minimize noise and obtain appropriate statistics.

Acknowledgements

Financial support was provided by the U.S. Department of Energy through Energy Materials Center at Cornell (EMC^2), NYSTAR, and the National Science Foundation. Special thank goes to Heather Edvenson for the synthesis of ordered intermetallic nanomaterials. The use of facilities in the Cornell Center for Materials Research, and C beam station, and F beam station at Cornell High Energy Syhcrotron Source (CHESS), are all gratefully acknowledged.

[1] G. Rupprechter, C. Weilach, *Nano Today* **2007**, *2*, 20–29.
[2] N. M. Markovic, P. N. Ross, *Surf. Sci. Rep.* **2002**, *45*, 117–229.
[3] *Handbook of Heterogeneous Catalysis* (Eds.: G. Ertl, H. Knözinger, F. Schüth, J. Weitkamp), Wiley-VCH, Weinheim, **1997**.
[4] G. A. Somorjai, *Introduction to Surface Chemistry and Catalysis*, Wiley, New York, **1994**.
[5] R. Schlögl, *Adv. Catal.* **2009**, *52*, 273–338.
[6] S. R. Bare, T. Ressler, *Adv. Catal.* **2009**, *52*, 339–465.
[7] E. H. Conrad, *Prog. Surf. Sci.* **1992**, *39*, 65–116.
[8] M. E. Gallagher, C. A. Lucas, V. Stamenkovic, N. M. Markovic, P. N. Ross, *Surf. Sci.* **2003**, *544*, L729L734.
[9] A. M. Venezia, *Catalysis Today* **2003**, *77*, 359–370.
[10] *X-ray Absorption Fine Structure for Catalysts and Surfaces* (Ed.: Y. Iwasawa), World Scientific, Singapore, **1996**.
[11] B. M. Weckhuysen, *In Situ Spectroscopy of Catalysts*, American Scientific Publishers, Stevenson Ranch, **2004**
[12] S. Mukerjee, J. Ziegelbauer, T. Arruda, D. Rmaker, B. Shyam, *Electrochem. Soc. Interface* **2008**, *17*, 46–52
[13] K. Tsuji, K. Nakano, H. Hayashi, K. Hayashi, C. Ro, *Anal. Chem.* **2008**, *80*, 4421–4454.
[14] P. Wobrauschek, *X-ray Spectrom.* **2007**, *36*, 289–300.
[15] C. Streli, *Appl. Spectro. Rev.* **2006**, *41*, 473–489.
[16] M. Mages, M. Óvári, W. Von Tümpling, K. Kröpfl, *Anal. Bioanal. Chem.* **2004**, *378*, 1095–1101.
[17] E. Hernandez-Caraballo, L. M. Macro-Parra, *Spectrochim. Acta Part B* **2003**, *58*, 2205–2213.
[18] S. Bouykens, C. Vazquez, *Spectrochim. Acta Part B* **2004**, *59*, 1189–1192.
[19] M. L. Carvalho, A. F. Marques, M. T. Lima, U. Reus, *Spectrochim. Acta Part B* **2004**, *59*, 1251–1257.
[20] C. L. Pearson, D. S. Dale, P. W. Brewer, P. I. Kuniholm, J. Lipton, S. W. Manning, *J. Arch. Sci.* **2009**, *36*, 1206–1214.
[21] A. R. Woll, J. Mass, C. Bisulca, R. Huang, D. H. Bilderback, S. Gruner, N. Gao, *Appl. Phys. A* **2006**, *83*, 235–238.
[22] E. Marguí, K. V. Meel, R. V. Grieken, A. Buendía, C. Fontà, M. Hidalgo, I. Queralt, *Anal. Chem.* **2009**, *81*, 1404–1410.
[23] E. Gebel, *Anal. Chem.* **2008**, *80*, 8862.
[24] K. Peeters, K. De Wael, L Vincze, A. Adriaens, *Anal. Chem.* **2005**, *77*, 5512–5519.
[25] K. Van Meel, A. Smekens, M. Behets, P. Kazandjian, R. Van Grieken, *Anal. Chem.* **2007**, *79*, 6383–6389.
[26] S. Sattayasamitsathit, J. Burdick, R. Bash, P. Kanatharana, P. Thavarungkul, J. Wang, *Anal. Chem.* **2007**, *79*, 7571–7575.
[27] J. Larminie, A. Dicks, *Fuel Cell Systems Explained*, 2nd ed., Wiley, New York, **2003**.
[28] C. L. Lamy, J.-M. Leger, S. Srinivasan in *Direct Methanol Fuel Cell: From a Twentieth Century Electrochemist's Dream to a Twenty-First Century Emerging Technology, Vol. 24* (Eds.: J. O'M. Brockris, B. E. Conway. R. E. White), Kluwer Academic/Plenum Publishers, New York, **2001**
[29] E. Reddington, A. Sapienza, B. Gurau, R. Viswanathan, S. Sarangapani, E. S. Smotkin, T. E. Mallouk, *Science* **1998**, *280*, 1735–1737.
[30] K. Scott, A. Shukla in *Modern Aspects of Electrochemistry, Vol. 40* (Ed.: R. E. White), Springer, New York, **2007**.
[31] J. Lipkowski, P. N. Ross, *Electrocatalysis*, Wiley-VCH, Weinheim, **1992**.
[32] M. Watanabe, S. Motoo, *J. Electroanal. Chem.* **1975**, *60*, 267–273.
[33] M. Watanabe, S. Motoo, *J. Electroanal. Chem.* **1975**, *60*, 275–283.
[34] E. Casado-Rivera, Z. Gál, A. C. D. Angelo, C. Lind, F. J. DiSalvo, H. D. Abruña, *ChemPhysChem* **2003**, *4*, 193–199.
[35] E. Casado-Rivera, D. J. Volpe, L. Alden, C. Lind, C. Downie, T. Vázquez-Alvarez, A. C. D. Angelo, F. J. DiSalvo, H. D. Abruña, *J. Am. Chem. Soc.* **2004**, *126*, 4043–4049.
[36] Y. Liu, H. Abe, H. M. Edvenson, T. Ghosh F. J. DiSalvo, H. D. Abruña, *Phys. Chem. Chem. Phys.* **2010**, DOI: 10.1039/C0CP00321B.
[37] Y. Liu, D. R. Blasini, F. J. DiSalvo, H. D. Abruña, unpublished results.
[38] Y. Liu, M. A. Lowe, F. J. DiSalvo, H. D. Abruña, J. Phys. Chem. C 114, 14929–14938.
[39] XPaXs software: XPaXS is a collection of python packages and libraries for X-ray science. This software is developed with the goal of providing useful real-time feedback and analysis of scanning XRF experiments. See: http://dale.chess.cornell.edu/~darren/xpaxs/.
[40] C. Roychowdhury, F. Matsumoto, V. B. Zeldovich, S. C. Warren, P. F. Mutolo, M. Ballesteros, U. Wiesner, H. D. Abruña, F. J. DiSalvo, *Chem. Mater.* **2006**, *18*, 3365–3372.
[41] PyMCA X-ray Fluorescence Toolkit: http://pymca.sourceforge.net/.
[42] *X-ray Data Booklet* (Ed.: A. Thompson et al.), Lawrence Berkeley National Laboratory, Berkeley, **2001**.

Received: May 5, 2010
Published online: October 13, 2010

